Materials Chemistry

Cite this: *J. Mater. Chem.*, 2011, **21**, 16344

www.rsc.org/materials

COMMUNICATION

Multifunctional Ag@Fe_2O_3 yolk–shell nanoparticles for simultaneous capture, kill, and removal of pathogen†

Zhanhua Wei,[a] Zijian Zhou,[a] Meng Yang,[a] Chenghong Lin,[b] Zhenghuan Zhao,[a] Dengtong Huang,[a] Zhong Chen[b] and Jinhao Gao*[a]

Received 2nd August 2011, Accepted 2nd September 2011
DOI: 10.1039/c1jm13691g

We combined silver and iron oxide nanoparticles to make unique Ag@Fe_2O_3 yolk–shell multifunctional nanoparticles by the Kirkendall effect. After the surface functionalization using glucose, the Ag@Fe_2O_3–Glu conjugates exhibited both high capture efficiency of bacteria and potent antibacterial activity. The Ag@Fe_2O_3 yolk–shell nanostructures may offer a unique multifunctional platform for simultaneous rapid detection and capture of bacteria and safe detoxification treatment.

The multidisciplinary developments in the fields of physics, chemistry, and biology have led to the rational design and use of multifunctional nanomaterials for biomedical applications, such as bacterial detection, cell imaging, diagnosis, and therapeutics.[1–3] Sensitive detection and efficient elimination of pathogenic bacteria are vital in human health and environmental safety, including prevention of infections, water purification, and biodefense. For example, *E. coli* O157:H7, a member of a class of pathogenic *E. coli* known as enterohemorrhagic *Escherichia coli* (EHEC), may produce shiga-like toxins and cause severe illness or even death. Recent advances in nanotechnology have developed many methods for rapid and sensitive bacterial detection[4–6] as well as different types of nanomaterials as potent antibacterial agents,[7–12] while the strategy on integration of pathogen detection and disinfection was rare. After the evaluation and confirmation of bacterial infection by sensitive detection, the powerful antiseptic treatments are needed immediately without the accessional contaminations, which are crucial in clinics and food safety.[13–15]

Magnetic nanoparticles have the advantages in bacterial detection and capture with a quick and sensitive manner.[16,17] However, the relatively moderate capture efficiency[5] and the remains of living bacteria may be unfavorable for the detoxification purpose, especially disinfection in clinics and water purification. The major drawback of chlorination in water purification is the highly toxic chlorine and the harmful chemical by-products in water.[18] So it is imperative to develop a safe and multimodal strategy for the rapid detection, killing, and elimination of bacteria from products. Silver (Ag) nanoparticles may be a promising alternative as a new potent and broad-spectrum antibacterial agent due to their ultrasmall size and unique chemical and physical properties.[7–9] In this communication, we combine advanced features of Ag and magnetic nanoparticles, design and synthesize a novel core–hollow–shell nanostructure with Ag nanoparticles as cores and iron oxide as shells, Ag@Fe_2O_3 yolk–shell nanoparticles, as a multifunctional platform to aim at detecting, killing, and eliminating pathogen (*e.g.*, *E. coli* O157:H7) without any accessional contaminations in a rapid and efficient manner.

The successful synthesis of maghemite hollow nanoparticles based on the oxidization of iron nanoparticles by the Kirkendall effect[19–21] speeds up the development of yolk–shell nanostructures using iron oxide as shells.[22–26] Using Ag nanoparticles (ESI, Fig. S1†) as the seeds, we directly injected $Fe(CO)_5$ into the solution of 1-octadecene containing oleylamine and Ag nanoparticles under an inert atmosphere, sequentially heated the solution at 250 °C in the presence of air for 2 hours, and finally obtained Ag@Fe_2O_3 yolk–shell nanoparticles by centrifugation. As shown in the transmission electron microscopy (TEM) image (Fig. 1a), the Ag@Fe_2O_3 yolk–shell

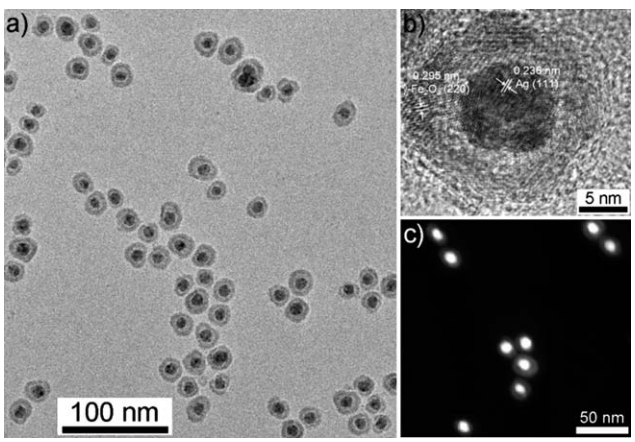

Fig. 1 (a) TEM, (b) HRTEM, and (c) STEM-HAADF images of Ag@Fe_2O_3 yolk–shell nanoparticles synthesized *via* the Kirkendall effect.

[a]*State Key Laboratory of Physical Chemistry of Solid Surfaces, The Key Laboratory for Chemical Biology of Fujian Province, and Department of Chemical Biology, College of Chemistry and Chemical Engineering, Xiamen University, Xiamen, 361005, China. E-mail: jhgao@xmu.edu.cn; Fax: +86-592-2189959; Tel: +86-592-2180278*
[b]*Department of Electronic Science and Fujian Key Laboratory of Plasma and Magnetic Resonance, Xiamen University, Xiamen, 361005, China*
† Electronic supplementary information (ESI) available: Detailed experimental procedures, TEM images, XPS analysis, UV-vis analysis, and antibacterial results on agar. See DOI: 10.1039/c1jm13691g

nanoparticles have the uniform structure with an obvious void between the Ag yolk and iron oxide shell. The size of Ag is about 8 nm in diameter and the thickness of iron oxide is roughly 3 nm. The size of Ag yolk and the thickness of the outer shell are controllable. It is noted that the shells are porous[23] and even partially broken as shown in TEM images (Fig. 1a and S1†) probably due to the Kirkendall effect and the mild etching by oleic acid in the synthesis.[27] The high-resolution TEM (HRTEM) image of Ag@Fe_2O_3 yolk–shell nanoparticles (Fig. 1b) indicates that both Ag yolk and iron oxide shell are crystalline. The iron oxide nanoshells are maghemite (γ-Fe_2O_3) phase with high polycrystallinity,[20] which was further confirmed by the selected area electron diffraction (SAED) pattern (ESI, Fig. S1†). The lattice spacing of 0.236 nm in Ag corresponds to the (111) lattice plane, and the lattice spacing of 0.295 nm in iron oxide corresponds to the (220) lattice plane of γ-Fe_2O_3. The scanning TEM with high angle annular dark field (STEM-HAADF) image (Fig. 1c) further confirms the uniform structure of Ag@Fe_2O_3 yolk–shell nanoparticles.

X-Ray photoelectron spectroscopic (XPS) measurement of Ag@Fe_2O_3 yolk–shell nanoparticles gives the signals of Fe(III) and Ag(0) in the spectra (ESI, Fig. S2†). Inductively coupled plasma atomic emission spectroscopy (ICP-AES) analysis indicates that the molar ratio of Ag and Fe_2O_3 is 6 : 5, corresponding to ~448 ng Ag per μg of Ag@Fe_2O_3 yolk–shell nanoparticles. The as-prepared Ag nanoparticles have the intense surface plasmon resonance (SPR) absorption at around 417 nm (ESI, Fig. S3†), which is the characteristic absorption peak of Ag nanoparticles.[28] Because the refractive index of iron oxide (2.3–3.1) is significantly higher than that of Ag (0.18), the presence of an iron oxide shell and its thickness should strongly affect the plasmon band position.[24] For example, the coating of an iron oxide shell (~3 nm in thickness) shifted the SPR of silver nanoparticles to about 506 nm (ESI, Fig. S3†).

The magnetic measurement reveals the superparamagnetism of Ag@Fe_2O_3 nanoparticles at room temperature. Standard zero-field-cooling (ZFC) and field-cooling (FC) measurements give the estimated blocking temperature of 110 K (Fig. 2a). The field-dependent magnetization measurement shows that Ag@Fe_2O_3 nanoparticles are superparamagnetic and the saturated magnetization (M_s) is about 24.8 emu g^{-1} particles (64.1 emu g^{-1} in terms of Fe) at room temperature (Fig. 2b), which is sufficient to allow the nanoparticles to be suitable for magnetic separation using a small magnet.[29–31] To test the MR transverse relaxation rate enhancement effects of Ag@Fe_2O_3 nanoparticles, we acquired multi-echo gradient echo images at a 7 tesla (T) MRI scanner. T_2-weighted MR images (Fig. 2c) showed that Ag@Fe_2O_3 nanoparticles have strong MR relaxation enhancement with the relaxivity value (r_2) of 58.1 mM^{-1} S^{-1} (ESI, Fig. S4†), indicating that Ag@Fe_2O_3 nanoparticles can be used as a T_2 MRI contrast agent.

We then did surface modification and functionalization of the nanoparticles using the conjugate of dopamine (DA) and carbohydrates (*e.g.*, glucose, galactose) because many bacteria use mammalian cell surface carbohydrates as anchors for attachments[5] and DA can be used as a robust anchor to present functional molecules on the surface of iron oxide nanostructures.[32,33] The conjugation of as-prepared Ag@Fe_2O_3 yolk–shell nanoparticles and monosaccharide molecules makes a new multifunctional nanomaterial in one nanoarchitecture, which could endow it with the ability of rapid detection and capture of bacteria as well as high antibacterial activity. Using Ag@Fe_2O_3–Glu conjugates as an example (Fig. 3a), we incubated

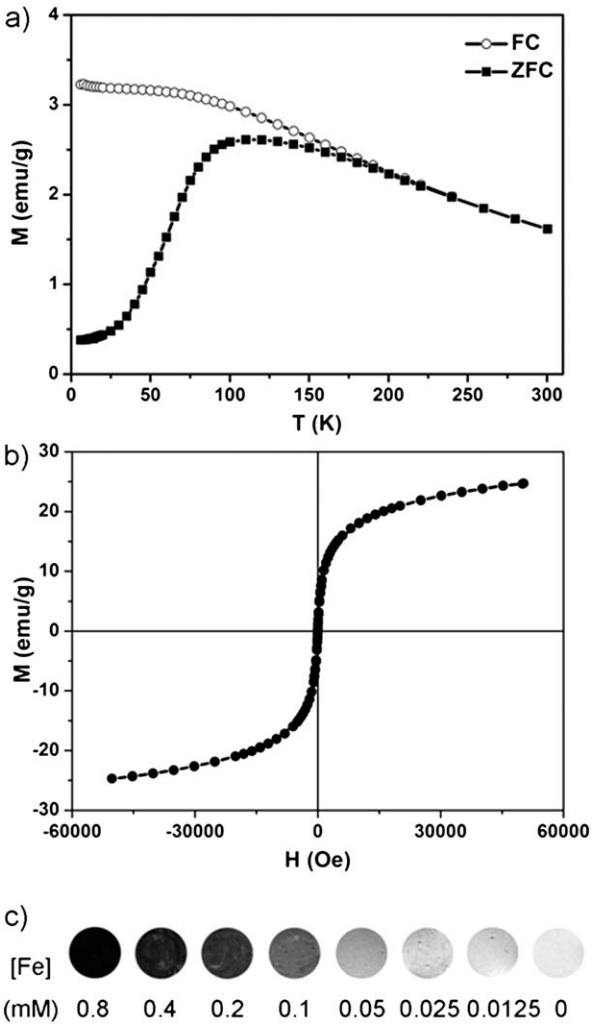

Fig. 2 (a) Temperature-dependence of the ZFC/FC magnetization (at a magnetic field of 100 Oe) and (b) room-temperature field-dependent magnetization measurement of Ag@Fe_2O_3 yolk–shell nanoparticles. (c) T_2-weighted MR images of Ag@Fe_2O_3 yolk–shell nanoparticles from a 7.0 T MRI system at different concentrations in water (containing 1% agarose gel).

E. coli ER2566 cells (10^7 colony forming units per mL, CFU mL^{-1}) with different amounts of the conjugates for 30 min. Because *E. coli* ER2566 was constructed of the recombinant plasmids encoding enhanced green fluorescent protein (EGFP), we measured the fluorescent intensity of each supernatant after the magnetic capture and separation (within 5 min) to evaluate the capture efficiency of bacteria. As shown in Fig. 3b, the fluorescent intensity of supernatants decreased dramatically as the concentration of Ag@Fe_2O_3–Glu conjugates increased, indicating that the number of captured bacteria increased. The capture efficiency could reach 97% when we use 64 μg mL^{-1} of Ag@Fe_2O_3–Glu conjugates and the use of 128 μg mL^{-1} of Ag@Fe_2O_3–Glu conjugates can remove almost all of the bacteria (≥99%; Fig. 3c). The high capture efficiency of Ag@Fe_2O_3–Glu conjugates indicated the strong interaction between the bacterial cell walls and the conjugates, which is promising for the rapid and efficient elimination of pathogenic bacteria from products. We used the TEM technique to detect the captured bacteria and observed the rod

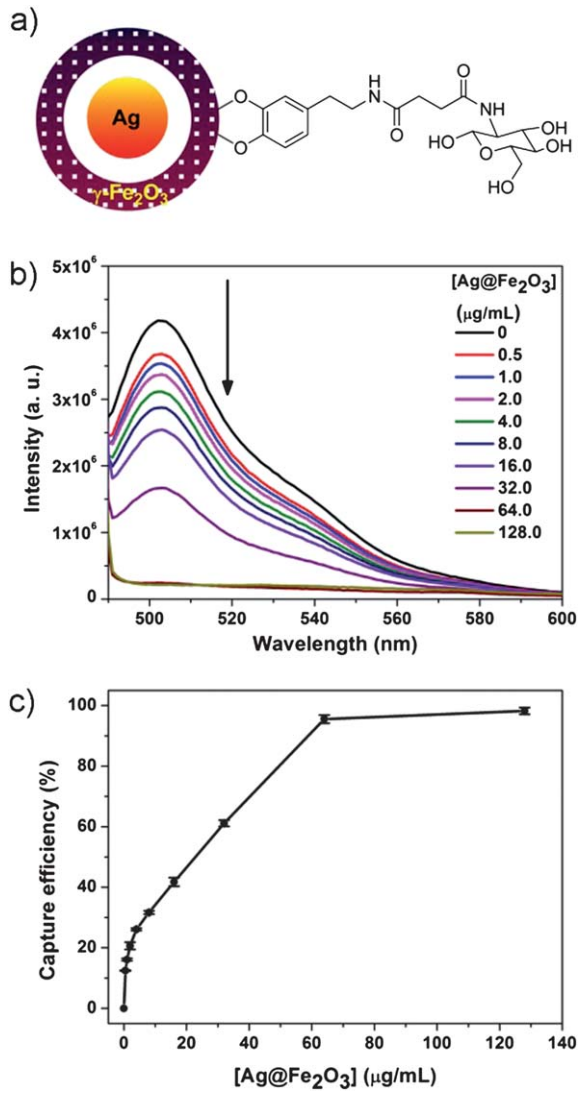

Fig. 3 (a) The schematic cartoon of glucose-modified $Ag@Fe_2O_3$ yolk–shell nanostructures ($Ag@Fe_2O_3$–Glu conjugates) using dopamine as an anchor. (b) The fluorescence analysis of the supernatants from *E. coli* ER2566 samples after treatment with different concentrations of $Ag@Fe_2O_3$–Glu conjugates (from top to down: 0, 0.5, 1.0, 2.0, 4.0, 8.0, 16.0, 32.0, 64.0, and 128.0 μg mL^{-1}). (c) The analysis of bacterial capture efficiency based on fluorescence measurements.

shape of bacteria (~2 μm in size) with many aggregations of nanoparticles on the bacterial cell walls (ESI, Fig. S5†), which agrees with the binding of $Ag@Fe_2O_3$–Glu conjugates with bacteria. The detection limit was approximately 60 CFU mL^{-1} using $Ag@Fe_2O_3$–Glu conjugates.

To test the antibacterial activity, we chose two representative types of strains as examples: Gram-negative bacteria *E. coli* O157:H7 and Gram-positive bacteria *Bacillus subtilis* (*B. subtilis*). We evaluated the *in vitro* antimicrobial activity by the serial two-fold agar dilution method and determined the minimum inhibitory concentration (MIC) of $Ag@Fe_2O_3$–Glu conjugates. The MIC values of $Ag@Fe_2O_3$–Glu conjugates for *E. coli* O157:H7 and *B. subtilis* are 15.2 μg mL^{-1} and 21.8 μg mL^{-1}, respectively (Table 1). Since even 150 μg mL^{-1} of glucose-modified γ-Fe_2O_3 hollow nanoparticles cannot

Table 1 MIC values of glucose-modified $Ag@Fe_2O_3$ yolk–shell and γ-Fe_2O_3 hollow nanoparticles on Gram-negative (*E. coli* O157:H7) and Gram-positive (*B. subtilis*) bacteria

	MIC/μg mL^{-1}		
	$Ag@Fe_2O_3$	In terms of Ag for $Ag@Fe_2O_3$	γ-Fe_2O_3 hollow
E. coli O157:H7	15.2	6.6	>150
B. subtilis	21.8	9.5	>150

inhibit bacterial growth (Table 1 and Fig. S6†), the Ag cores should play a key role in killing bacteria. $Ag@Fe_2O_3$–Glu conjugates showed high antibacterial activity with low MIC values in terms of Ag (6.6 μg mL^{-1} and 9.5 μg mL^{-1} for *E. coli* O157:H7 and *B. subtilis*, respectively), which is comparative to previous reports on the antibacterial study of Ag nanoparticles.[34,35] According to the presence of multiple antibacterial mechanisms of Ag nanoparticles[8] and the unique yolk–shell structure[22,23] of $Ag@Fe_2O_3$–Glu conjugates, we proposed the probable mechanism as follows. $Ag@Fe_2O_3$–Glu conjugates can specifically target the surfaces of bacteria because of the strong binding between glucose and bacterial cell wall, which results in the high attachment of nanoparticles on bacterial surfaces. The porous and partially broken iron oxide shells may facilitate the silver ions and/or silver nanoparticles to release from shells, interact with bacteria, disrupt the bacterial cell walls and membranes, and lead to the death of bacteria. We indeed observed iron oxide hollow nanostructures without Ag cores in the captured bacterial samples (ESI, Fig. S5†), which directly supports our proposed mechanism. Core–shell nanostructures, normally synthesized by sequential growth methods at high temperature (*e.g.*, $FePt@Fe_3O_4$ and $Pt@Fe_3O_4$ core–shell nanoparticles[23]), have a stable and compact shell to prevent the core from contacting with the outside environment, which results in the inert property of core. Unlike the core–shell nanostructures, yolk–shell nanoparticles *via* the Kirkendall effect have three advanced and important features: porous shells, hollow structure between the core and shell, and "naked" cores without surface protection,[22,23] which allow Ag yolks to interact with the outside species and ensure $Ag@Fe_2O_3$ yolk–shell nanoparticles to have strong antibacterial properties.

Because $Ag@Fe_2O_3$–Glu conjugates have both excellent capture efficiency of bacteria and high antibacterial activity, we did the bacterial elimination experiment from drinking water to investigate the disinfection effect. After the incubation of contaminated water (10^7 CFU mL^{-1} of *E. coli* ER2566 or *E. coli* O157:H7 as testing examples, Fig. 4a and d) with $Ag@Fe_2O_3$–Glu conjugates (60 μg mL^{-1}) for about 30 min, the supernatants and precipitates were collected by magnetic separation immediately and imprinted on the agar plates. After 24 h of incubation at 37 °C, we did not observe any bacterial strains on the agar (Fig. 4), indicating that there is not any living bacterium in the supernatants and the captured bacteria in precipitates are also dead. The results demonstrate that the $Ag@Fe_2O_3$–Glu conjugate is an excellent candidate as novel and potent biocides to kill the pathogenic bacteria efficiently and remove them simultaneously. The combination of these two capabilities may dramatically improve the disinfection treatment (*i.e.*, not only killing the bacteria but also reducing the amount of toxins generated by bacteria after magnetic separation) and warrant the biosafety against pathogenic bacteria. Moreover, we observed a trace amount of Ag

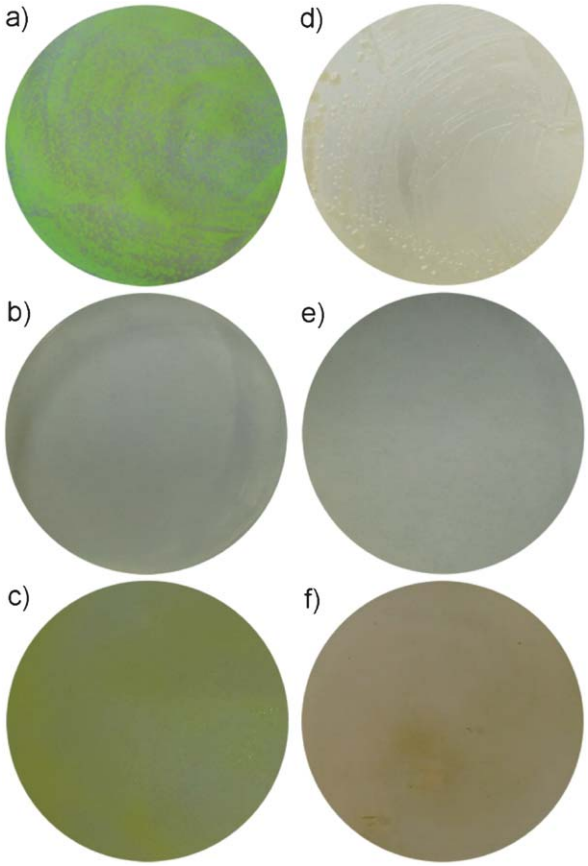

Fig. 4 The experimental results of bacterial elimination from contaminated drinking water. The agar plate images of water containing EGFP-encoded *E. coli* ER2566 (10^7 CFU mL^{-1}) (a) before and (b) after treatment using Ag@Fe_2O_3–Glu conjugates. The agar plate images of water containing *E. coli* O157:H7 (10^7 CFU mL^{-1}) (d) before and (e) after treatment using Ag@Fe_2O_3–Glu conjugates. The agar plate images of precipitates (captured bacteria and aggregations of nanoparticles) after magnetic separation from water containing (c) *E. coli* ER2566 and (f) *E. coli* O157:H7 using Ag@Fe_2O_3–Glu conjugates. All samples were incubated at 37 °C for 24 h.

left in the supernatant by ICP-AES (as low as the detection limit) probably because the Ag nanoparticles along with iron oxide nanoshells and Ag ions inside bacteria can be removed by the magnetic separation, so the potential toxicity issue of Ag nanoparticles may be absent after the process of decontamination treatment, which is an additional advantage over other present antibacterial methods, such as the use of Ag nanoparticles alone.[36]

In summary, we have synthesized a uniform multifunctional nanostructure, Ag@Fe_2O_3 yolk–shell nanoparticles, with a red-shifted SPR absorption and strong magnetic contrast enhancement effect. After the surface functionalization using glucose, the Ag@Fe_2O_3–Glu conjugates exhibited both high capture efficiency of bacteria because of specific targeting and strong magnetic properties and potent antibacterial activity due to the Ag cores. The use of other specific molecules (*e.g.*, peptides and antibodies) is also feasible for targeting modification. The investigation of such multifunctional nanostructures may lead to the development of other types of nanomaterials as novel antibacterial agents.[37,38] The Ag@Fe_2O_3 yolk–shell nanostructures may offer a unique multifunctional platform for simultaneous rapid detection of bacteria and safe decontamination treatment, which may have attractive applications in water purification and food safety.

We are thankful to National Science Foundation of China (21021061, 81000662), the Fundamental Research Funds for the Central Universities (2010121012), and Program for New Century Excellent Talents in University (NCET-10-0709) for the financial support.

Notes and references

1 J. R. McCarthy and R. Weissleder, *Adv. Drug Delivery Rev.*, 2008, **60**, 1241–1251.
2 J. Cheon and J. H. Lee, *Acc. Chem. Res.*, 2008, **41**, 1630–1640.
3 J. H. Gao, H. W. Gu and B. Xu, *Acc. Chem. Res.*, 2009, **42**, 1097–1107.
4 R. L. Phillips, O. R. Miranda, C.-C. You, V. M. Rotello and U. H. F. Bunz, *Angew. Chem., Int. Ed.*, 2008, **47**, 2590–2594.
5 K. El-Boubbou, C. Gruden and X. F. Huang, *J. Am. Chem. Soc.*, 2007, **129**, 13392–13393.
6 H. Lee, T.-J. Yoon and R. Weissleder, *Angew. Chem., Int. Ed.*, 2009, **48**, 5657–5660.
7 J. R. Morones, J. L. Elechiguerra, A. Camacho, K. Holt, J. B. Kouri, J. T. Ramirez and M. J. Yacaman, *Nanotechnology*, 2005, **16**, 2346–2353.
8 K. Chaloupka, Y. Malam and A. M. Seifalian, *Trends Biotechnol.*, 2010, **28**, 580–588.
9 H. L. Cao, X. Y. Liu, F. H. Meng and P. K. Chu, *Biomaterials*, 2011, **32**, 693–705.
10 J. Lellouche, E. Kahana, S. Elias, A. Gedanken and E. Banin, *Biomaterials*, 2009, **30**, 5969–5978.
11 K. R. Raghupathi, R. T. Koodali and A. C. Manna, *Langmuir*, 2011, **27**, 4020–4028.
12 A. Travan, C. Pelillo, I. Donati, E. Marsich, M. Benincasa, T. Scarpa, S. Semeraro, G. Turco, R. Gennaro and S. Paoletti, *Biomacromolecules*, 2009, **10**, 1429–1435.
13 C. D. Hillyer, C. D. Josephson, M. A. Blajchman, J. G. Vostal, J. S. Epstein and J. L. Goodman, *Hematology*, 2003, 575–589.
14 M. Koopmans, C. H. von Bonsdorff, J. Vinje, D. de Medici and S. Monroe, *FEMS Microbiol. Rev.*, 2002, **26**, 187–205.
15 M. Loretz, R. Stephan and C. Zweifel, *Food Control*, 2011, **22**, 347–359.
16 H. W. Gu, K. M. Xu, C. J. Xu and B. Xu, *Chem. Commun.*, 2006, 941–949.
17 J. H. Gao, L. Li, P. L. Ho, G. C. Mak, H. W. Gu and B. Xu, *Adv. Mater.*, 2006, **18**, 3145–3148.
18 K. Gopal, S. S. Tripathy, J. L. Bersillon and S. P. Dubey, *J. Hazard. Mater.*, 2007, **140**, 1–6.
19 S. Peng and S. H. Sun, *Angew. Chem., Int. Ed.*, 2007, **46**, 4155–4158.
20 A. Cabot, V. F. Puntes, E. Shevchenko, Y. Yin, L. Balcells, M. A. Marcus, S. M. Hughes and A. P. Alivisatos, *J. Am. Chem. Soc.*, 2007, **129**, 10358–10360.
21 J. H. Gao, B. Zhang, X. X. Zhang and B. Xu, *Angew. Chem., Int. Ed.*, 2006, **45**, 1220–1223.
22 J. H. Gao, G. L. Liang, B. Zhang, Y. Kuang, X. X. Zhang and B. Xu, *J. Am. Chem. Soc.*, 2007, **129**, 1428–1433.
23 J. H. Gao, G. L. Liang, J. S. Cheung, Y. Pan, Y. Kuang, F. Zhao, B. Zhang, X. X. Zhang, E. X. Wu and B. Xu, *J. Am. Chem. Soc.*, 2008, **130**, 11828–11833.
24 E. V. Shevchenko, M. I. Bodnarchuk, M. V. Kovalenko, D. V. Talapin, R. K. Smith, S. Aloni, W. Heiss and A. P. Alivisatos, *Adv. Mater.*, 2008, **20**, 4323–4329.
25 Q. K. Ong, X.-M. Lin and A. Wei, *J. Phys. Chem. C*, 2011, **115**, 2665–2672.
26 S. Cheong, P. Ferguson, K. W. Feindel, I. F. Hermans, P. T. Callaghan, C. Meyer, A. Slocombe, C.-H. Su, F.-Y. Cheng, C.-S. Yeh, B. Ingham, M. F. Toney and R. D. Tilley, *Angew. Chem., Int. Ed.*, 2011, **50**, 4206–4209.
27 K. Cheng, S. Peng, C. J. Xu and S. H. Sun, *J. Am. Chem. Soc.*, 2009, **131**, 10637–10644.
28 X. Z. Lin, X. Teng and H. Yang, *Langmuir*, 2003, **19**, 10081–10085.

29 L. Wang, Z. M. Yang, J. H. Gao, K. M. Xu, H. W. Gu, B. Zhang, X. X. Zhang and B. Xu, *J. Am. Chem. Soc.*, 2006, **128**, 13358–13359.
30 J. H. Gao, W. Zhang, P. B. Huang, B. Zhang, X. X. Zhang and B. Xu, *J. Am. Chem. Soc.*, 2008, **130**, 3710–3711.
31 H. Chen, C. Deng and X. Zhang, *Angew. Chem., Int. Ed.*, 2010, **49**, 607–611.
32 C. J. Xu, K. M. Xu, H. W. Gu, R. K. Zheng, H. Liu, X. X. Zhang, Z. H. Guo and B. Xu, *J. Am. Chem. Soc.*, 2004, **126**, 9938–9939.
33 C. J. Xu, J. Xie, D. Ho, C. Wang, N. Kohler, E. G. Walsh, J. R. Morgan, Y. E. Chin and S. H. Sun, *Angew. Chem., Int. Ed.*, 2008, **47**, 173–176.
34 L. Kvitek, A. Panacek, J. Soukupova, M. Kolar, R. Vecerova, R. Prucek, M. Holecova and R. Zboril, *J. Phys. Chem. C*, 2008, **112**, 5825–5834.
35 A. Panacek, L. Kvitek, R. Prucek, M. Kolar, R. Vecerova, N. Pizurova, V. K. Sharma, T. Nevecna and R. Zboril, *J. Phys. Chem. B*, 2006, **110**, 16248–16253.
36 X. Chen and H. J. Schluesener, *Toxicol. Lett.*, 2008, **176**, 1–12.
37 V. Sambhy, M. M. MacBride, B. R. Peterson and A. Sen, *J. Am. Chem. Soc.*, 2006, **128**, 9798–9808.
38 M. L. Pang, J. Y. Hu and H. C. Zeng, *J. Am. Chem. Soc.*, 2010, **132**, 10771–10785.

